The Astrophysical Journal, 778:129 (13pp), 2013 December 1 doi:10.1088/0004-637X/778/2/129

THE ROLE OF GALAXY INTERACTION IN THE SFR–M_* RELATION: CHARACTERIZING MORPHOLOGICAL PROPERTIES OF *Herschel*-SELECTED GALAXIES AT $0.2 < z < 1.5$

Chao-Ling Hung (洪肇伶)[1], D. B. Sanders[1], C. M. Casey[1], N. Lee[1], J. E. Barnes[1], P. Capak[2], J. S. Kartaltepe[3], M. Koss[1], K. L. Larson[1], E. Le Floc'h[4], K. Lockhart[1], A. W. S. Man[1,5], A. W. Mann[1], L. Riguccini[6,7], N. Scoville[8], and M. Symeonidis[9,10]

[1] Institute for Astronomy, University of Hawaii, 2680 Woodlawn Drive, Honolulu, HI 96822, USA; clhung@ifa.hawaii.edu
[2] Spitzer Science Center, MS 314-6, California Institute of Technology, Pasadena, CA 91125, USA
[3] National Optical Astronomy Observatory, 950 North Cherry Avenue, Tucson, AZ 85719, USA
[4] UMR AIM (CEA-UP7-CNRS), CEA-Saclay, Orme des Merisiers, bât. 709, F-91191 Gif-sur-Yvette Cedex, France
[5] Dark Cosmology Centre, Niels Bohr Institute, University of Copenhagen, Denmark
[6] NASA Ames Research Center, Moffett Field, CA, USA
[7] BAER Institute, Santa Rosa, CA, USA
[8] California Institute of Technology, MC 249-17, 1200 East California Boulevard, Pasadena, CA 91125, USA
[9] University of Sussex, Department of Physics and Astronomy, Pevensey 2 Building, Falmer, Brighton BN1 9QH, Sussex, UK
[10] University College London, Department of Space & Climate, Mullard Space Science Laboratory, Holmbury St. Mary, Dorking RH5 6NT, Surrey, UK
Received 2013 June 3; accepted 2013 September 16; published 2013 November 12

ABSTRACT

Galaxy interactions/mergers have been shown to dominate the population of IR-luminous galaxies ($L_{\rm IR} \gtrsim 10^{11.6}\ L_\odot$) in the local universe ($z \lesssim 0.25$). Recent studies based on the relation between galaxies' star formation rates and stellar mass (the SFR–M_* relation or the "galaxy main sequence") have suggested that galaxy interaction/mergers may only become significant when galaxies fall well above the galaxy main sequence. Since the typical SFR at a given M_* increases with redshift, the existence of the galaxy main sequence implies that massive, IR-luminous galaxies at high z may not necessarily be driven by galaxy interactions. We examine the role of galaxy interactions in the SFR–M_* relation by carrying out a morphological analysis of 2084 *Herschel*-selected galaxies at $0.2 < z < 1.5$ in the COSMOS field. Using a detailed visual classification scheme, we show that the fraction of "disk galaxies" decreases and the fraction of "irregular" galaxies increases systematically with increasing $L_{\rm IR}$ out to $z \lesssim 1.5$ and $z \lesssim 1.0$, respectively. At $L_{\rm IR} > 10^{11.5}\ L_\odot$, $\gtrsim$50% of the objects show evident features of strongly interacting/merger systems, where this percentage is similar to the studies of local IR-luminous galaxies. The fraction of interacting/merger systems also systematically increases with the deviation from the SFR–M_* relation, supporting the view that galaxies falling above the main sequence are more dominated by mergers than the main-sequence galaxies. Meanwhile, we find that $\gtrsim$18% of massive IR-luminous "main-sequence galaxies" are classified as interacting systems, where this population may not evolve through the evolutionary track predicted by a simple gas exhaustion model.

Key words: galaxies: evolution – galaxies: structure – infrared: galaxies

Online-only material: color figures

1. INTRODUCTION

In the hierarchical structure formation paradigm, interactions of galaxies are essential in driving galaxy growth and transforming galaxy morphology (White & Rees 1978; Barnes & Hernquist 1992). During violent encounters of galaxies, gas in disk galaxies loses its angular momentum and falls toward the center, inducing enhanced star formation (Barnes & Hernquist 1996). The UV light emitted from newborn massive stars is scattered and absorbed by dust and then re-emitted in the far-IR. In the local universe ($z \lesssim 0.3$), the majority of ultraluminous infrared galaxies (ULIRGs; $L_{\rm IR}$[11] $\geqslant 10^{12}\ L_\odot$) and a significant portion of luminous infrared galaxies (LIRGs; $10^{11}\ \leqslant L_{\rm IR} \leqslant\ 10^{12}\ L_\odot$) are triggered by major mergers (Sanders & Mirabel 1996) of gas-rich disks, as is evident by their morphological features, such as bridges and tidal tails, and complex kinematics (e.g., Veilleux et al. 2002; Colina et al. 2005). These luminous mergers may represent a crucial transition phase from gas-rich disk galaxies to quasi-stellar objects (Sanders et al. 1988). Although (U)LIRGs are rare locally, they contribute a significant amount of the star formation rate (SFR) density at high z (e.g., ∼70% at $z \sim 1$; Le Floc'h et al. 2005; Casey et al. 2012), implying that galaxy interactions play a dominant role in the cosmic star formation history if the origins of local and high-z (U)LIRGs are similar.

Nonetheless, the discovery of a tight correlation between galaxies' SFR and stellar mass (M_*, also known as the galaxy "main sequence" (MS); Brinchmann et al. 2004; Noeske et al. 2007b; Elbaz et al. 2007) has invoked an alternative picture of galaxy growth incorporating two distinct modes of star formation. The "normal star-forming mode" describes galaxies falling on the SFR–M_* relation evolving through secular processes such as gas accretion (e.g., Dekel et al. 2009a; Davé et al. 2010), while the "starburst mode" describes galaxies falling well above the MS that are likely driven by major mergers, representing a starbursting period with respect to the galaxies on the MS (Rodighiero et al. 2011). In this scenario, secular accretion in gaseous disks can drive high SFRs in massive galaxies, implying that the majority of (U)LIRGs are not driven by galaxy interactions at high z. Furthermore, the presence and tightness of the MS over a wide redshift range suggest that the star formation histories of galaxies can be simply parameterized based on gas exhaustion/regulation models (e.g., Noeske et al. 2007a;

[11] $L_{\rm IR} \equiv\ L_{8-1000\ \mu{\rm m}}$ in the object rest frame.

Bouché et al. 2010), where major mergers play a minor role on the MS.

An efficient way to determine the relative importance of galaxy interactions and secular accretion in high-z galaxies is through the characterization of their morphological properties. For example, high-resolution optical images taken with the Advanced Camera for Surveys (ACS) on board the *Hubble Space Telescope* (*HST*) as part of the Cosmic Evolution Survey (COSMOS; Scoville et al. 2007) covering $\sim$2 deg^2 can be used to analyze many thousands of galaxies. In terms of optical morphology, interacting systems often show dramatically different characteristics than isolated disk galaxies. Mergers may begin as close pairs without any sign of interaction, then display disrupted structures, tidal features, and finally coalesce (see Barnes & Hernquist 1992). Indeed, these different merger stages are seen out to $z \sim$ 1–2 in the COSMOS *HST*-ACS images (Kartaltepe et al. 2010a, 2012). Meanwhile, secular accretion from cold gas streams may result in clumpy substructure in gas-rich disks (Dekel et al. 2009a), which may explain some of the irregular structures observed in high-z galaxies (Elmegreen et al. 2004, 2007; Förster Schreiber et al. 2011).

How do these morphological properties relate to galaxy IR luminosity, stellar mass, and location on the SFR–M_* plane? Among the local (U)LIRGs, the increase in $L_{\rm IR}$ corresponds to the increasing merger fractions of galaxies and the progression of merger stages, from separated galaxy pairs and strongly disturbed interacting systems to more advanced mergers (e.g., Veilleux et al. 2002; Ishida 2004; Haan et al. 2011; Ellison et al. 2013, K. L. Larson et al., in preparation). However, it remains unclear if major mergers are also responsible for driving high SFR (e.g., (U)LIRGs) at high z. Kartaltepe et al. (2010b) show that the fraction of interacting systems systematically increases with $L_{\rm IR}$ at $z \sim 1$, which is similar to the trends seen in the local (U)LIRGs. Kartaltepe et al. (2012) perform a sophisticated visual classification of 52 ULIRGs at $z \sim 2$ (with a significant fraction of them lying on the MS) and find that 50% of them are dominated by interaction/merger systems (73% including irregular disks). However, Wuyts et al. (2011b) find that galaxies on the MS have a median Sérsic index of $n = 1$ and the Sérsic index increases for objects above and below the MS, implying that disk-like galaxies dominate the MS and mergers only dominate those galaxies falling well above the MS.

To understand these results based on different approaches and to examine the role of galaxy interactions in the SFR–M_* relation, we have carried out a morphological analysis of 2084 *Herschel*-selected galaxies at $0.2 < z < 1.5$ in the COSMOS 2 deg^2 field and explored how galaxy morphology varies with $L_{\rm IR}$ and distance from the MS. This sample is about twice as large as (three times larger at $1.0 < z < 1.5$) the previous *Spitzer* 70 μm identified sample (Kartaltepe et al. 2010a) and is also less biased by active galactic nuclei (AGNs) since it selects galaxies at longer wavelengths. We describe the data and sample selection in Section 2 and present our analysis and visual classification scheme in Section 3. In Section 4, we discuss galaxy morphological properties in three redshift bins. We discuss the implications of our results in Sections 5 and 6. Throughout this paper, we adopt a ΛCDM cosmology with $H_0 = 70$ km s^{-1} Mpc^{-1}, $\Omega_M = 0.3$, and $\Omega_\Lambda = 0.7$ (Hinshaw et al. 2009). Magnitudes are given in the AB system.

2. DATA AND SAMPLE SELECTION

The sources studied in this work are identified by the Photodetector Array Camera and Spectrometer (PACS; Poglitsch et al. 2010) and the Spectral and Photometric Imaging REceiver (SPIRE; Griffin et al. 2010) on board the *Herschel Space Observatory* (Pilbratt et al. 2010). The PACS (100 and 160 μm) and SPIRE (250, 350, and 500 μm) observations in the COSMOS field are acquired as part of the PACS Evolutionary Probe program (PEP; Lutz et al. 2011) and the Herschel Multi-tiered Extragalactic Survey (HerMES; Oliver et al. 2012). The beam sizes at 100, 160, 250, 350, and 500 μm are 8″, 12″, 18″, 25″, and 36″, respectively.

The photometries of PACS and SPIRE observations are performed at positions of known MIPS 24 μm sources (Le Floc'h et al. 2009) and Very Large Array 1.4 GHz sources (Schinnerer et al. 2010). This cross-identification source extraction (XID) is described in detail in Roseboom et al. (2010, 2012). A 3σ detection at 100, 160, 250, 350, and 500 μm corresponds to $\sim$ 5, 10, 8, 11, and 13 mJy, respectively (Roseboom et al. 2010; Berta et al. 2011). The *Herschel* photometry measurements are then cross-correlated to their K_s-band counterparts using a matching radius of 2″, and then cross-correlated to the full UV–near-IR multiwavelength data set in the COSMOS field using a matching radius of 1″ (Capak et al. 2007; Ilbert et al. 2009; McCracken et al. 2010; Lee et al. 2013, hereafter L13). Photometric redshifts and stellar masses for $\sim$70% of the *Herschel*-selected detections are thus known from their optical counterparts (Ilbert et al. 2009, 2010). Another 20% do not have reliable photometric redshifts (the majority of these sources fall in the masked area of the optical images), and the remaining 10% are completely obscured in optical images.

L13 measure the IR luminosity ($L_{\rm IR}$), dust temperature, and dust mass by fitting the IR spectral energy distribution (SED) of each *Herschel*-detected source to a coupled modified graybody and mid-IR power law (method described in Casey 2012). To ensure secure *Herschel* detections that are necessary for accurate SED fitting, L13 restrict the sample to those sources with $\geqslant$5 σ detections in at least two out of the five *Herschel* PACS and SPIRE bands and those with photometric redshifts. They find no apparent selection effects in dust temperature based on these signal-to-noise ratio limits. With this restriction, L13 identify a sample of 3457 sources spanning the redshift range $0 < z < 3.5$ and luminosity range $2 \times 10^8\ L_\odot \leqslant L_{\rm IR} \leqslant 3.8 \times 10^{13}\ L_\odot$.

3. ANALYSIS

3.1. Characterization of Herschel-selected Galaxies

We study the morphology of the *Herschel*-selected galaxies identified by L13 at $0.2 < z < 1.5$. We use the ACS F814W (I-band) images taken as part of the COSMOS survey (Koekemoer et al. 2007). The sample is split into three redshift bins: $0.2 < z < 0.5$, $0.5 < z < 1.0$, and $1.0 < z < 1.5$, where the observed I band corresponds to rest-frame V, B, and U bands, respectively. Given that band shifting between these three redshift bins may complicate any discussion of morphology evolution, we restrict our discussion of galaxy morphology to each redshift bin separately without addressing evolutionary trends with redshift.

A total of 2084 galaxies are analyzed in this study, with 676, 859, and 549 galaxies at $0.2 < z < 0.5$, $0.5 < z < 1.0$, and $1.0 < z < 1.5$. Figure 1 shows the distribution of *Herschel*-selected galaxies in $L_{\rm IR}$ and I-band magnitude for each redshift bin. Although our sample contains relatively few IR-luminous galaxies in the lowest redshift bin compared to the other two bins, the data in each redshift bin span a wide range with

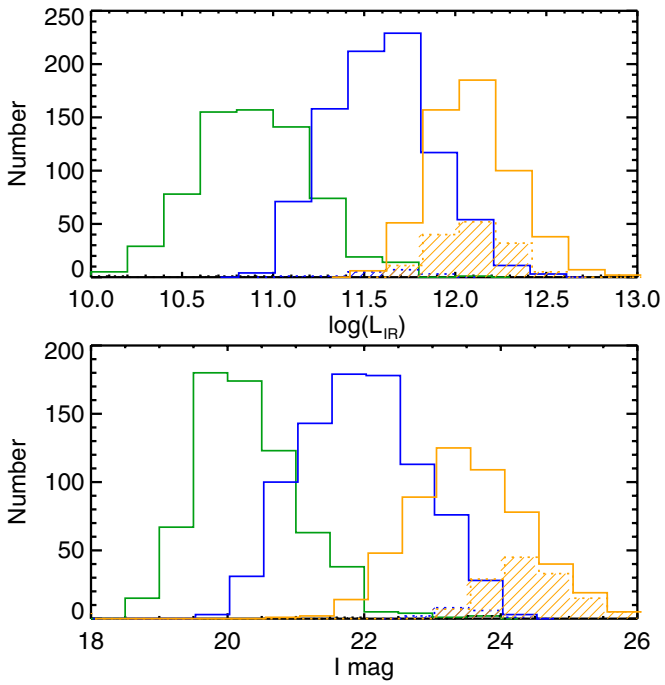

Figure 1. Distribution of *Herschel*-selected galaxies included in this study in L_{IR} and I-band magnitude. Green, blue, and orange indicate three redshift bins: $0.2 < z < 0.5$, $0.5 < z < 1.0$, and $1.0 < z < 1.5$. The shaded area illustrates the distribution of unclassifiable objects in each redshift bin. Note that although the histograms for different redshift bins have exactly the same location, the distributions are offset slightly from each other in the plot for clarity.

(A color version of this figure is available in the online journal.)

respect to the SFR–M_* relation, which allows us to probe the morphology on and above the galaxy MS. The shaded area illustrates the distribution of unclassifiable galaxies (described later in Section 3.2). The population of unclassifiable galaxies is mostly confined to the highest redshift bin ($1.0 < z < 1.5$), and these sources are often very faint in ($I > 24$). Since the fraction of unclassifiable galaxies is relatively small (except for the highest redshift bin), we expect that the unclassifiable galaxies play a minor role in global statistics even if they are biased toward a specific class of sources.

3.2. Visual Classification Scheme

We visually classify the morphological properties of 2084 *Herschel*-selected galaxies at $0.2 < z < 1.5$. In addition to the F814W I-band images, we also use the F125W (J-band) and F160W (H-band) images taken with the *HST* Wide Field Camera 3 (WFC3) as part of CANDELS (Cosmic Assembly Near-infrared Deep Extragalactic Legacy Survey; Grogin et al. 2011). CANDELS covers ∼6% of the COSMOS field, and only 72 galaxies in the WFC3 coverage meet on *Herschel* selection criteria (18 at $0.2 < z < 0.5$, 37 at $0.5 < z < 1.0$, and 17 at $1.0 < z < 1.5$). The J- and H-band images allow us to estimate the impact of measuring morphology using different rest-frame wavelengths. We classify galaxies based on their 50 kpc × 50 kpc images, where the corresponding angular sizes of image cutouts are determined from the photometric redshifts of the *Herschel* galaxies. Note that the variation of the 50 kpc scale with uncertain photo-z is small at $z > 0.2$.

The contrast and brightness schemes used to display the ACS images are critical for identifying morphological features. We apply two scaling schemes for each image, both of which are used for classifications: (1) an image displayed with logarithmic scaling and adjustable brightness and contrast; (2) an image with inverse hyperbolic sine stretch and fixed maximum and minimum values. The first image is used to demonstrate overall galaxy structure, and the second image is optimized for revealing faint structures.

We adopt the visual classification scheme used by the CANDELS team (Kartaltepe et al. 2012; Kocevski et al. 2012), with some minor modifications. For each galaxy, we identify its morphology class as disk, spheroid, irregular, or unclassifiable. One galaxy can be classified into more than one morphology class, such as irregular disks or spheroid with irregular features. The morphology class has a total of eight possible outcomes: disk, spheroid, irregular, disk + spheroid, disk + irregular, spheroid + irregular, disk + spheroid + irregular, and unclassifiable. In addition to the morphology class, we further assign an interaction class for each galaxy as either merger, interacting pair (major or minor), non-interacting pair (major or minor), or non-interacting galaxy. Figure 2 provides real examples of each morphology and interaction class in the three redshift bins.

The identification of features associated with galaxy interactions is based on the interaction/merger systems observed in the local universe (e.g., Surace et al. 1998; Veilleux et al. 2002). For example, two overlapping disks with disturbed features, obvious single or double nuclei, prominent tidal tails, bridges, and loops are all evidence of interactions (e.g., Toomre & Toomre 1972). However, the classification of galaxies with "clumpy structures," but no large-scale interacting features, can be ambiguous. In general, we classify galaxies with symmetric clump distributions as disk-like galaxies. We introduce an additional "ambiguous flag" for galaxies with asymmetric clump distribution; these objects may be candidates for secular-evolving clumpy disks (Elmegreen et al. 2004, 2007; Dekel et al. 2009b), or, alternatively, they may also be interacting systems whose large-scale tidal features have faded away.

3.3. Robustness of the Visual Classification

Throughout this work, the statistical results of galaxy morphology are based on the classification done by CLH, who perform detailed visual classifications for 2084 *Herschel*-selected galaxies. However, to address the reliability of these classification results based on one classifier, we enlist seven additional classifiers (hereafter the visual classification team, or the Team) to independently classify a subset of 248 galaxies at $0.5 < z < 1.5$, where this subset is uniformly distributed in L_{IR} but otherwise randomly selected. To combine the results of the individual classifications in the Team, we only assign morphology and interaction classes to galaxies when more than half of the Team members agree, which results in 242 galaxies in morphology class and 180 galaxies in interaction class. We compare the classification results between CLH and the Team in this subset in Figures 3 and 4. For the morphology class, CLH and the Team completely agree for 46% of the sample (indicated as orange cells in Figure 3). The agreement becomes 76% when including those cases where only one morphological feature is in disagreement (indicated as yellow cells in Figure 3). The agreement for interaction class is 75% (indicated as orange cells in Figure 4). We compare the statistical results of the morphology classes as a function of L_{IR} between CLH (2084 galaxies) and the Team (250 galaxies) in Figure 5. In general, the classification of disk and irregular features is consistent, while the spheroid classification yields larger uncertainties.

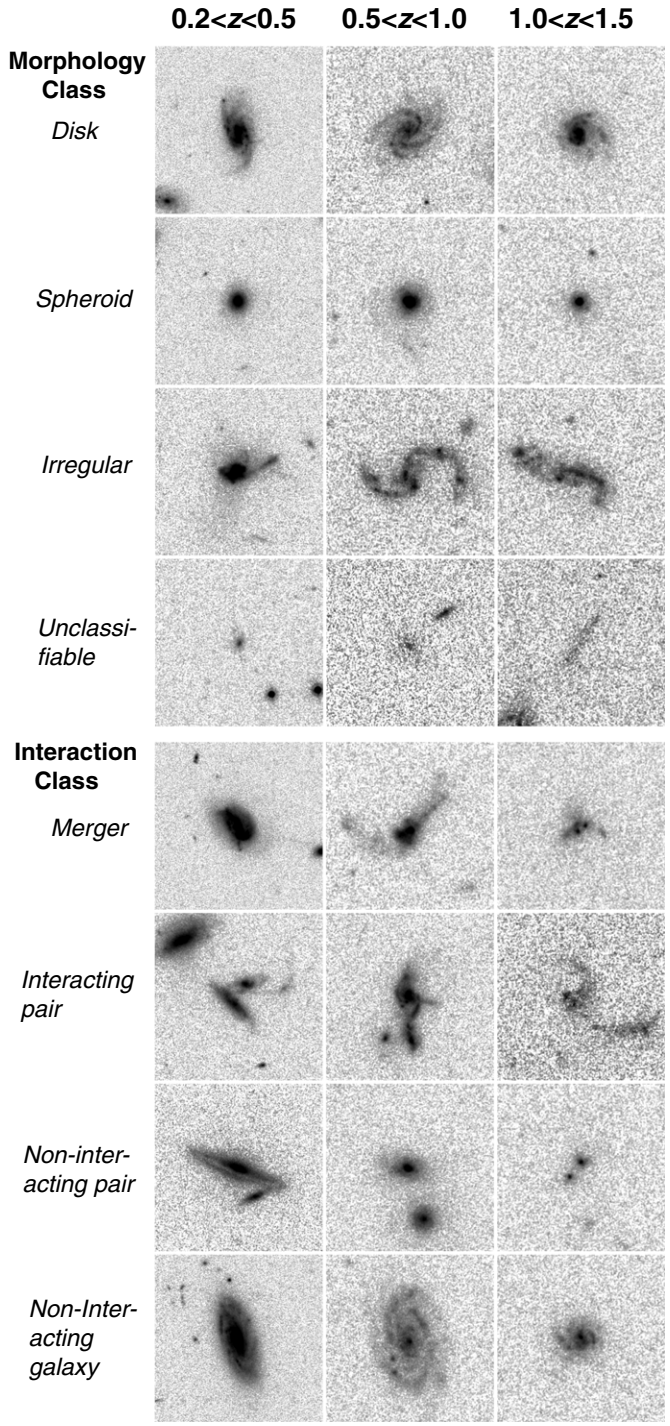

Figure 2. Examples of morphology classes and interaction classes in three redshift bins: $0.2 < z < 0.5$, $0.5 < z < 1.0$, and $1.0 < z < 1.5$. Note that the morphology classes provided here are classified as pure disk, pure spheroid, and irregular-only galaxies, but in practice galaxies can be classified as having multiple morphology classes.

In the results presented later, we combine morphology and interaction classes into six possible outcomes, including merger and major interacting pair, pure spheroid, non-interacting disk, non-interacting pair, minor interacting pair, and unclassifiable galaxy. We demonstrate our classification by presenting a subset of randomly selected examples in the Appendix, and we also examine the reliability of our classification results, again using this randomly selected subset.

Team (242 galaxies)

CLH (242 galaxies)	D	S	I	D+S	D+I	S+I	D+S+I	U
D	42	6	7	2	7	1	0	0
S	0	9	1	0	0	4	0	0
I	3	1	34	0	3	2	0	0
D+S	25	7	2	9	4	0	0	0
D+I	9	2	10	0	10	1	0	0
S+I	0	1	2	0	0	0	0	0
D+S+I	3	1	3	0	3	1	0	0
U	0	2	16	0	1	0	0	8

Cells for which CLH and the Team agree with all features
Cells for which CLH and the Team only disagree with one feature

Figure 3. Comparison between CLH and the Team's classification results in a subset of galaxies. This table categorizes all eight possible outcomes in the classification of morphology classes, including D (disk only), S (spheroid only), I (irregular only), D+S (disk and spheroid), D+I (disk and irregular), S+I (spheroid and irregular), D+S+I (disk, spheroid, and irregular), and U (unclassifiable). The table lists the number of galaxies in each cell as belonging to the certain category classified by CLH and the Team. For illustration, orange cells indicate the categories where CLH and the Team completely agree with all of the morphological features, and yellow cells indicate the categories where only one morphological feature is in disagreement. Adding the numbers in orange and yellow cells, about 76% agreement in morphology class is achieved between CLH and the Team.

(A color version of this figure is available in the online journal.)

Team (180 galaxies)

CLH (180 galaxies)	Mer	Int	Pair	Non
Mer	16	6	0	3
Int	4	13	1	3
Pair	3	12	15	2
Non	8	2	4	88

Cells for which CLH and the Team agree

Figure 4. Comparison between CLH and the Team's classification results in a subset of galaxies. This table categorizes four possible outcomes in the classification of interaction classes, which includes Mer (merger), Int (interacting pair), Pair (non-interacting pair), and Non (non-interacting galaxy). The table lists the number of galaxies in each cell as belonging to the certain category classified by CLH and the Team. For illustration, orange cells indicate complete agreement between CLH and the Team. Adding the numbers in orange cells, about 75% agreement in interaction class is achieved between CLH and the Team.

(A color version of this figure is available in the online journal.)

4. RESULTS

4.1. Morphological Properties of Herschel-selected Galaxies

In this section, we examine the fraction of objects represented by each morphology class (disk, spheroid, and irregular) as a

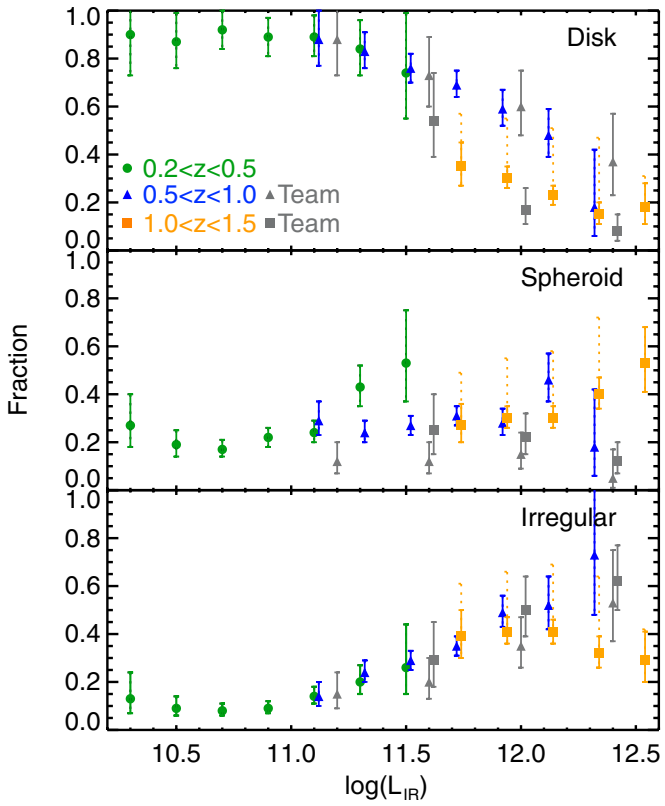

Figure 5. Relation between each morphology class (disk, spheroid, and irregular) and $L_{\rm IR}$ in the entire sample of 2084 *Herschel*-selected galaxies. Galaxies in three redshift bins at $0.2 < z < 0.5$, $0.5 < z < 1.0$, and $1.0 < z < 1.5$ are shown as the green circles, blue triangles, and orange squares, respectively. The gray symbols indicate the classification results of 250 galaxies done by the Team. The error bars in solid lines are determined assuming a Poisson distribution. The upper error bars shown as dashed lines represent the fraction of unclassifiable galaxies in each $L_{\rm IR}$ bin (the most conservative estimates of uncertainties). Note that the data points for different redshift bins are offset slightly from each other (in $L_{\rm IR}$) for clarity.

(A color version of this figure is available in the online journal.)

function of $L_{\rm IR}$. We use a bin size of 0.2 dex in $L_{\rm IR}$, which represents the typical uncertainties in $L_{\rm IR}$ measurements. Most of the $L_{\rm IR}$ bins contain more than 50 galaxies. We present the statistical results in three redshift bins. The $0.5 < z < 1.0$ bin provides the widest coverage in $L_{\rm IR}$ ($10^{11.0} \lesssim L_{\rm IR} \lesssim 10^{12.5}\ L_\odot$), whereas the lowest (highest) redshift bin covers the low (high) luminosity end.

Figure 5 shows that the fraction of galaxies with disk features systematically decreases with $L_{\rm IR}$, and the fraction of those with irregular features systematically increases with $L_{\rm IR}$. These trends are most clearly seen in the two lower redshift bins, $0.2 < z < 0.5$ and $0.5 < z < 1.0$. As $L_{\rm IR}$ increases from $10^{11.0}$ to $10^{12.3}\ L_\odot$, the disk fraction decreases from ~0.9 to ~0.2 and the irregular fraction increases from ~0.1 to ~0.7. In the highest redshift bin ($1.0 < z < 1.5$), the low disk fraction at high $L_{\rm IR}$ ($\gtrsim 10^{12.2}\ L_\odot$) and the high irregular fraction at $10^{11.6} \lesssim L_{\rm IR} \lesssim 10^{12.2}\ L_\odot$ are consistent with the two lower redshift bins. However, compared to the two lower redshift bins, the disk fraction in the highest redshift bin is systematically lower at $10^{11.6} \lesssim L_{\rm IR} \lesssim 10^{12.2}\ L_\odot$, and the irregular fraction is systematically lower at $L_{\rm IR} \gtrsim 10^{12.2}\ L_\odot$. The fraction of galaxies with prominent spheroid features shows a slight increasing trend with increasing $L_{\rm IR}$ in all redshift bins. The spheroid fraction remains 0.2–0.3 in most of the $L_{\rm IR}$ bins but increases to ~0.5 at $L_{\rm IR} \sim 10^{12.5}\ L_\odot$.

The discrepancies in disk and irregular fractions between the two lower redshift bins and the highest one may partly originate from band shifting, in which the F814W band traces the rest-frame U band at $z > 1$ and does not necessarily resemble the optical morphology. For example, Cameron et al. (2011) show that ~25% of massive galaxies (above $10^{10}\ M_\odot$) at $1.5 < z < 2.15$ are regular disks at their rest-frame optical wavelengths despite their highly irregular features at UV. The fainter UV light and severe surface brightness dimming further desensitize visual classifications at $z > 1$, leading to ~30% of unclassifiable galaxies.

We have compared our results with the galaxy morphology study that is based on a *Spitzer* 70 μm-selected sample in the COSMOS field (Kartaltepe et al. 2010b, hereafter K10). The *Spitzer* 70 μm observations identified 1503 galaxies spanning the redshift range $0.01 < z < 3.5$, with a median redshift of 0.5. *Herschel* observations have allowed us to enlarge the sample of IR-luminous galaxies by a factor of two at $0.5 < z < 1.0$ and by a factor of three at $1.0 < z < 1.5$. In K10, the fraction of spirals among all 1503 galaxies shows a clear decreasing trend with $L_{\rm IR}$ (Figure 4 in K10), which is consistent with the disk fraction seen in our *Herschel*-selected sample in the two lower redshift bins. We note that ~80% of the *Spitzer* 70 μm selected galaxies are at $z < 1$, and thus the trends presented in the entire sample mostly reflect the sample at $z < 1$. As for the comparison with spheroid features in the *Herschel*-selected galaxies, a slight increasing trend with $L_{\rm IR}$ is also seen in K10 (the sum of ellipticals and QSOs). Overall, the correlations between morphological class and $L_{\rm IR}$ are consistent between the current *Herschel*-selected galaxies and the previous *Spitzer* 70 μm selected galaxies.

4.2. The Distribution of Interacting Systems

Here, we examine the fraction of interacting systems as a function of $L_{\rm IR}$ and relative offset from the SFR–M_* "MS" relation. For each galaxy, we use the redshift-dependent SFR–M_* relation corresponding to the galaxy redshift. We adopt a functional form of the SFR–M_* relation from Bouché et al. (2010):

$$\mathrm{SFR} = 150\ M_{*,11}^{p}(1+z)_{3.2}^{q}\ M_\odot\ \mathrm{yr}^{-1}, \quad (1)$$

where $M_{*,11} \equiv M_*/10^{11}\ M_\odot$, $(1+z)_{3.2} \equiv (1+z)/3.2$, $p \simeq 0.8$, and $q \simeq 2.7$ in the redshift range $z = 0$–2. To relate $L_{\rm IR}$ to the SFR–M_* relation, we convert $L_{\rm IR}$ to SFR through

$$\mathrm{SFR_{UV+IR}}[M_\odot\ \mathrm{yr}^{-1}] \simeq \mathrm{SFR_{IR}} = 1.09 \times 10^{-10}(L_{\rm IR}/L_\odot) \quad (2)$$

(Kennicutt 1998; Wuyts et al. 2011a), where $\mathrm{SFR_{IR}}$ represents the reprocessed light from newborn stars and $\mathrm{SFR_{UV}}$ represents the unobscured UV light. In this conversion, we assume that unobscured UV light is negligible in these *Herschel*-identified dusty galaxies (Howell et al. 2010). Also, we do not account for any AGN contribution, which may be significant at the order of 25% at $L_{\rm IR} > 10^{12}\ L_\odot$(Veilleux et al. 1995; Koss et al. 2013).

Figure 6 shows the fraction of interacting systems (the sum of mergers and major interacting pairs) as a function of $L_{\rm IR}$. The fraction of interacting systems shows a clear increasing trend with $L_{\rm IR}$ in the two lower redshift bins, and it reaches ~0.5 at $L_{\rm IR} > 10^{11.5}\ L_\odot$. Our results show the same trend as the "Major Mergers" in K10, with a rapid increase at $L_{\rm IR} \sim 10^{11.5}\ L_\odot$.

To examine the role of galaxy interactions in the SFR–M_* relation, we further investigate the dependence of the interaction fraction with distance from the SFR–M_* relation, measured along the $L_{\rm IR}$ axis. The *Herschel*-selected sample spans from

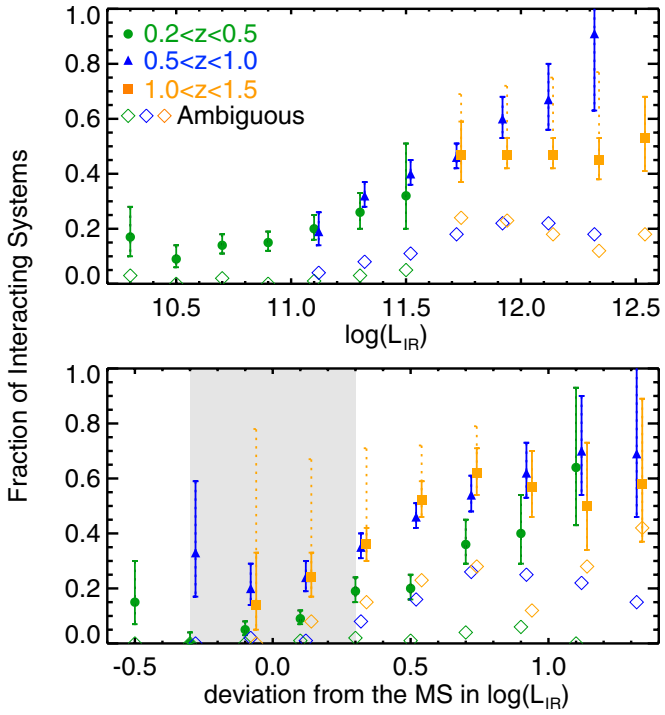

Figure 6. Fraction of interacting systems as a function of L_{IR} and the deviation from the SFR–M_* relation. As in Figure 5, galaxies in three redshift bins at $0.2 < z < 0.5$, $0.5 < z < 1.0$, and $1.0 < z < 1.5$ are shown as the green circles, blue triangles, and orange squares, respectively. The gray area in the bottom panel illustrates the location of galaxy main sequence with a typical dispersion of 0.3 dex. The error bars in solid lines are determined assuming a Poisson distribution. The upper error bars shown as the dashed lines represent the fraction of unclassifiable galaxies in each L_{IR} bin (the most conservative estimates of uncertainties). The diamonds represent the ambiguous galaxies that are identified as interacting systems due to their irregular and clumpy structure without the presence of large-scale tidal features. Note that data points for different redshift bins are offset slightly from each other (in L_{IR}) for clarity.
(A color version of this figure is available in the online journal.)

0.2 dex below to 1.2 dex above the SFR–M_* relation in each redshift bin. Given a typical dispersion of 0.3 dex in the SFR–M_* relation (Noeske et al. 2007b), this sample covers galaxies falling on the MS through 4σ outliers. The bottom panel of Figure 6 shows an increasing trend that is similar to the trend with L_{IR}, where the fraction of interacting galaxies increases from ~0.2 on the MS to ~0.5 as the deviation achieves ~0.5 dex. Taking the $0.5 < z < 1.0$ bin, the correlation between the interaction fraction and L_{IR} is only slightly stronger than the correlation with the distance from the SFR–M_* relation (correlation coefficient of 0.98 versus 0.93 with standard errors of 0.09 and 0.13). Such similar trends are expected since the distance from the SFR–M_* relation is a function of L_{IR}. We further calculate the percentage of interacting systems along the galaxy MS by including galaxies falling within the typical dispersion of 0.3 dex in the SFR–M_* relation (e.g., Noeske et al. 2007b). At $0.2 < z < 1.5$, ~18% (±2%) of the massive ($10^{10} M_\odot < M_* < 10^{11} M_\odot$) IR-luminous galaxies falling on the MS are classified as interacting systems. In comparison, ~51% (±3%) of the MS galaxies are classified as non-interacting disks. The percentage of interacting MS galaxies is larger in the two higher redshift bins (~27% ± 4% and ~26% ± 5%) compared to the lowest redshift bin (~8% ± 2%).

In the top left panel of Figure 7, we plot the percentage of interacting systems on the basis of L_{IR} and M_*. This plot illustrates the correlations in Figure 6 in a two-dimensional view. The fraction of interacting systems increases fairly uniformly with L_{IR} at all observed M_*. The rest of the panels in Figure 7 show results for the remainder of our objects that are not classified as interacting systems, including spheroid-only, non-interacting disk, non-interacting pair, minor interacting pair, and unclassifiable. The sum of each L_{IR} and M_* bin adds up to 100% over all six panels. The distribution of non-interacting disks shows a decreasing trend with L_{IR}, and no clear trends are seen in the other four panels. The pure spheroids may be explained as late stage or the end product of mergers, and the non-interacting pairs may be the beginning stage of mergers. However, since these categories do not show clear evidence of interaction, we choose not to combine them with interacting systems or non-interacting disks.

We have quantified the uncertainties in the interaction fraction when different criteria are used (the ambiguous flag). About 25% of interacting galaxies are also assigned as ambiguous class, and they do not show distinct distribution compared to the entire interacting systems (Figure 6). The majority of candidates of high-z clumpy disks lie well above the SFR–M_* relation as other unambiguously classified interacting systems.

4.3. The Comparison between F814W, F125W, and F160W Morphologies

Seventy-two *Herschel*-selected galaxies have WFC3 F125W- and F160W-band images from CANDELS (Grogin et al. 2011; Koekemoer et al. 2011; 18 at $0.2 < z < 0.5$, 37 at $0.5 < z < 1.0$, and 17 at $1.0 < z < 1.5$), and thus we can compare the morphology in F814W, F125W, and F160W of these galaxies. We see no obvious differences between the F125W and F160W images; hereafter, we only use the F125W images for our discussion due to their better spatial resolution.

In the lowest redshift bin, all galaxies preserve the same classifications between F814W and F125W images except for three galaxies that show more prominent spheroid components at the longer wavelength. At $0.5 < z < 1.0$, the overall fraction of disk features from these two bands is similar, but we see a higher percentage of spheroid features (16% versus 37%) and a lower percentage of irregular features (40% versus 20%) from the classifications based on the F125W images. In the highest redshift bin where the F814W images probe the rest-frame U band, a higher percentage of disk features (30% versus 60%) and lower percentage of irregular features (60% versus 35%) are observed with F125W images. As for the interaction class, about 20%–30% of galaxies at $0.5 < z < 1.5$ have different classifications. About half of these high-redshift objects show less clumpy structure in the F125W images, and they tend to be recognized as non-interacting galaxies (but we also notice that the lower resolution F125W images compared to F814W images can smooth out detailed structures). In the other half, the secondary companion or large tidal features are only detected at longer wavelengths, thus increasing the interaction fraction. In the highest redshift bin, two unclassifiable objects in F814W images are both classified as interacting galaxies.

The differences seen between the F814W and F125W images for these 72 galaxies demonstrate the difficulty in studying galaxy morphology using only one band, particularly in between rest-frame UV and optical. The morphological features can vary due to band shifting, especially when identifying disk features at $z > 1$ and irregular features at $z > 0.5$. However, we emphasize that this work has split the entire sample into three redshift bins that correspond to

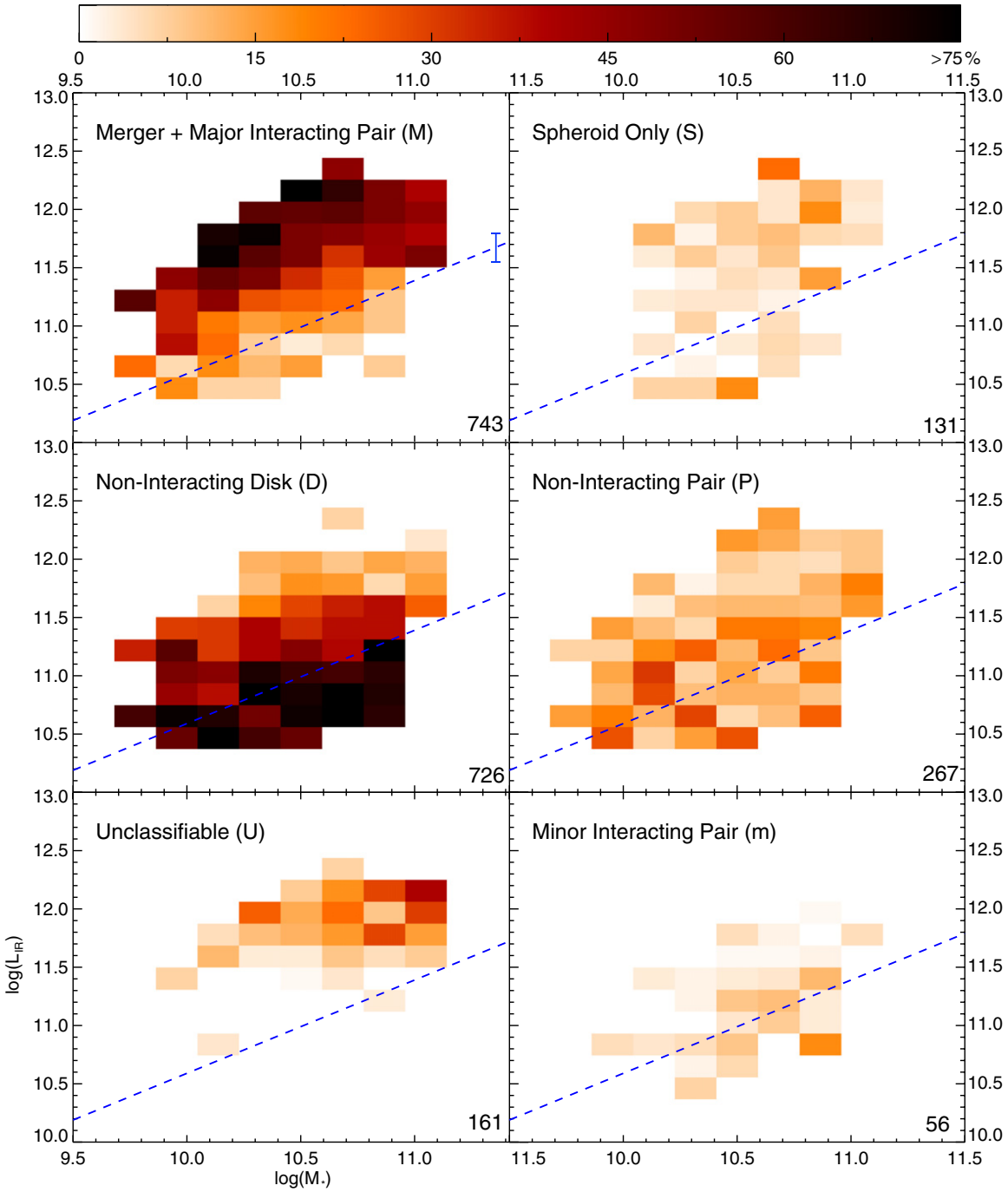

Figure 7. Six panels show the percentage of merger+major interacting pair, spheroid only, non-interacting disk, non-interacting pair, unclassifiable, and minor interacting pair. Each $L_{\rm IR}$ and M_* bin adds up to 100% in all six panels. The letters in the brackets correspond to the morphology classification results indicated in Figures 8–11. The numbers in the bottom right corner of each panel indicate the numbers of galaxies of each category. The increasing trend with $L_{\rm IR}$ seen in the top left panel shows similar information as the top panel in Figure 6 since the dependence of the interaction fraction on M_* is small. The blue dashed line in each panel is the SFR–M_* relation at the median redshift ($z = 0.7$) of the entire sample, and the corresponding error bar in the top left panel indicates the dispersion of the SFR–M_* relation within $z = 0.7 \pm 0.2$ redshift range.

(A color version of this figure is available in the online journal.)

rest-frame V, B, and U bands, and we focus on investigating how galaxy morphologies vary with their intrinsic properties ($L_{\rm IR}$, M_*, and the location on the SFR–M_* relation) in each redshift bin. Within individual redshift bins, any morphological trend does not vary strongly with redshift. The impact from band shifting on our conclusions should only be significant if the band-shifting effects are strongly correlated with $L_{\rm IR}$ and M_*.

5. DISCUSSION

5.1. The Role of Interaction in the SFR–M_* Relation

By investigating the morphological properties of 2084 *Herschel*-detected galaxies at $0.2 < z < 1.5$, we can address two important issues about high-z star-forming and starburst galaxies. (1) How do galaxy morphologies (which hint at the

physical mechanisms that drive star formation) correlate with intrinsic galactic properties such as L_{IR} and M_*? (2) What is the role of galaxy interactions in driving star formation and starburst activity at $z \sim 1$?

In Figure 6, the fraction of interactions shows clear increasing trends with both L_{IR} and the distance from the SFR–M_* relation. Such an increasing trend with L_{IR} is consistent with the findings for (U)LIRGs in the local universe (e.g., Ishida 2004) and for the *Spitzer* 70 μm selected galaxies at $z \sim 1$ (Kartaltepe et al. 2010b), in which interacting systems/mergers become dominant at higher L_{IR}. The increasing trends with distance from the SFR–M_* relations further demonstrate the growing role of galaxy interaction with increasing L_{IR} regardless of different stellar mass ($10^{10} \lesssim M_* \lesssim 10^{11}\,M_\odot$). Such an increasing trend of merger fraction with respect to the distance from the galaxy MS is also reported in Hα-selected samples at lower SFR and lower M_* ends (Stott et al. 2013). The morphological analysis of local (U)LIRGs shows that merger stage is correlated with increasing L_{IR}, from separated galaxy pairs, to strongly disturbed interacting systems, to more advanced mergers (Veilleux et al. 2002; Ishida 2004; Haan et al. 2011; Ellison et al. 2013, K. L. Larson et al., in preparation). At $z \sim 1$, we see the same increasing trends in the percentage of interacting systems with increasing L_{IR} (this work and K10), suggesting that mergers also play an important role in driving IR luminosity at higher z.

Are galaxy interactions only important when galaxies fall well above the SFR–M_* relation in contrast to the normal star-forming, MS galaxies? Based on the logarithmic distributions of BzK-selected and PACS-selected galaxies at $1.5 < z < 2.5$, Rodighiero et al. (2011) conclude that only 2% of star-forming galaxies represent high SFR outliers (i.e., starbursts, which are likely driven by major merger events) with respect to Gaussian-distributed MS galaxies. However, without morphology information, it remains unclear if all galaxies on the MS are evolving via secular accretion and only off-MS galaxies are interacting/merger systems. In this work, we probe galaxy morphology on and well above the MS at $z \sim 1$ based on 2084 *Herschel*-selected galaxies. We determine that the percentage of interacting systems along the MS is ~18% (±3%) given a typical dispersion of 0.3 dex in the SFR–M_* relation (e.g., Noeske et al. 2007b) in comparison to the ~51% non-interacting disk MS galaxies. The percentage remains significant (~15%) even if we exclude galaxies with ambiguous classifications that can be explained as either clumpy disks or interacting galaxies. In fact, this percentage can be even higher (~25%) if some of the unclassifiable systems are interacting/merging galaxies. This percentage (15%–25%) is similar to the findings at $z \sim 2$, in which ~24% (±4%) of MS galaxies (±0.3 dex) are interactions/mergers based on a sample of 122 (U)LIRGs (Kartaltepe et al. 2012, hereafter K12). This interacting/MS population may evolve through a merger-driven evolutionary sequence (e.g., Mihos & Hernquist 1996; Hopkins et al. 2006) instead of following the evolutionary tracks predicted by secular gas exhaustion/regulation models (Noeske et al. 2007a; Bouché et al. 2010).

5.2. Comparisons with Morphological Analysis Based on Sérsic Index

Wuyts et al. (2011b) use Sérsic index to characterize morphology for ~130,000 galaxies at $z \sim 1$, including galaxies in the COSMOS field. They study galaxy morphology on the basis of SFR and M_* and find a "structural MS" that has a Sérsic index of $n \sim 1$ along the MS and an increasing Sérsic index as the distance from the MS increases ($n = 1$ gives the exponential profile and $n = 4$ gives the de Vaucouleurs profile; Sérsic 1963). The increasing trend of Sérsic index with respect to the distance from the MS suggests that galaxies build up a central concentration of stellar mass as SFR increases at any M_*. One possible physical mechanism to drive such a transition of morphology is through galaxy interactions/mergers, where much of the gas content of the disk galaxies falls toward the center during galaxy encounters, and the violent relaxation re-distributes stars into a near de Vaucouleurs (Sérsic index $n = 4$) distribution (e.g., Toomre & Toomre 1972; Barnes & Hernquist 1992). This interpretation is consistent with the increasing fraction of interacting systems with respect to the distance from the MS seen in the bottom panel of Figure 6.

The structural MS with a Sérsic index of $n \sim 1$ implies that the MS galaxies mainly show disk-like structures and may be explained as "normal" star-forming galaxies. This conclusion is somewhat contradictory compared to the significant fraction of interacting MS galaxies identified in our work and K12. However, we emphasize that the results based on both analyses are not necessarily in disagreement. This can be due to the difficulties in translating Sérsic index and morphological type, particularly for interacting systems. Although Sérsic index may be a good proxy for disk galaxies ($n = 1$) and elliptical galaxies ($n = 4$), it does not accurately represent interacting systems due to its parametric form (Lotz et al. 2004). For example, the automatic Sérsic index fitting algorithm often fails to identify interacting pairs. Furthermore, galaxy interactions can result in messy and clumpy structures, which often yield a small Sérsic index since the overall light distribution is even flatter than that in normal disks. To illustrate this statement, we have measured the Sérsic index of 36 local (U)LIRGs, all of which show clear signatures of interactions from GOALS-SDSS images (The Great Observatories All-Sky LIRG Survey; Armus et al. 2009). We find a median Sérsic index of 1.8 for these 36 galaxies, which include all merger stages (C.-L. Hung et al., in preparation). Given the complications in translating Sérsic index to galaxy morphology types, we favor conclusions based on visual classifications.

6. CONCLUSIONS

We have carried out a detailed morphological analysis of a large sample of 2084 *Herschel*-selected (PACS + SPIRE) galaxies with redshifts $0.2 < z < 1.5$ in the full 2 deg^2 COSMOS field. A detailed visual classification scheme is employed to classify each object (e.g., disk, spheroid, irregular, strong interaction/merger). We then compare the distribution of morphological types with L_{IR}, as well as distance above and below the SFR–M_* relation ("galaxy MS"). Our conclusions are summarized below.

1. The percentage of galaxies classified as "disks" decreases systematically with increasing L_{IR} at all values of M_*, whereas the percentage of objects classified as "irregular" systematically increases with L_{IR}.
2. The percentage of strongly interacting/merger systems increases with L_{IR}, as well as distance above the SFR–M_* relation, with ~50% of galaxies classified as interacting/merger systems at $L_{IR} > 10^{11.5}\,L_\odot$.
3. We also find that a significant percentage ($\gtrsim$18%) of the IR-luminous, MS galaxies (±0.3 dex) show signatures of strong interaction/mergers, suggesting that this population

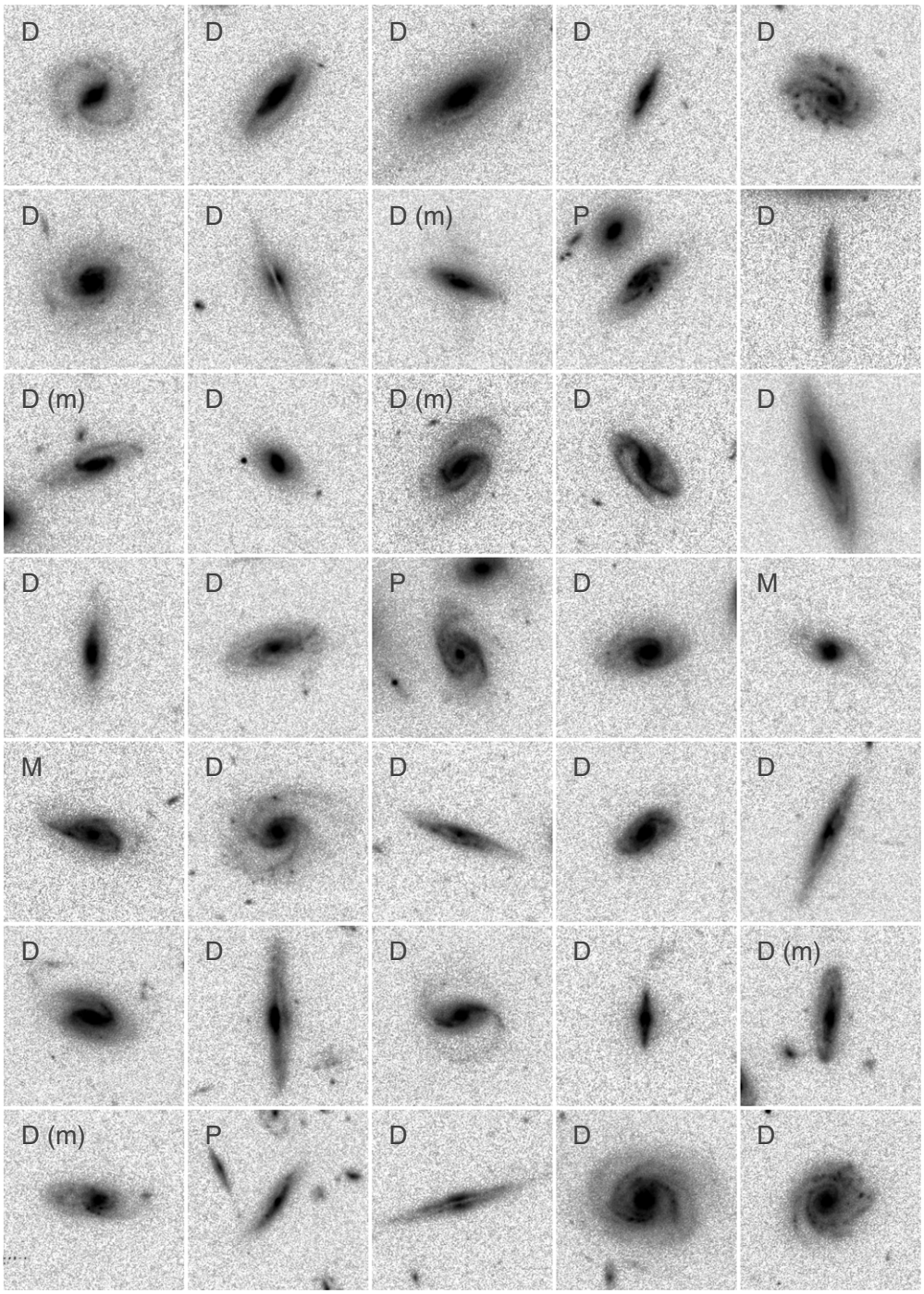

Figure 8. ACS F814W-band image gallery of randomly selected, *Herschel*-selected galaxies at $0.37 < z < 0.45$ with $M_* > 10^{10.5}\ M_\odot$ and $L_{\rm IR} < 10^{11}\ L_\odot$. The length and width of each image correspond to a physical size of 50 kpc and an angular size of $\sim 7''$ at $z = 0.7$. The classification results (corresponding to the six panels in Figure 7, are indicated in the top left corner (M: merger or major interacting pair, S: spheroid only, D: non-interacting disk, P: non-interacting pair, U: unclassifiable, m: minor interacting pair). The possible alternative classifications are shown in brackets.

may not evolve through the evolutionary tracks predicted by simple gas exhaustion models.

C.-L. Hung thanks V. U and J. Chu for their help with visual classification at the early stage of this project. D. B. Sanders and C. M. Casey acknowledge the hospitality of the Aspen Center for Physics, which is supported by the National Science Foundation grant No. PHY-1066293. C. M. Casey is generously supported by a Hubble Fellowship from Space Telescope Science Institute, grant HST-HF-51268.01-A.

COSMOS is based on observations with the NASA/ESA *Hubble Space Telescope*, obtained at the Space Telescope Science Institute, which is operated by AURA, Inc., under NASA contract NAS 5-26555; also based on data collected at the Subaru Telescope, which is operated by the National Astronomical Observatory of Japan; *XMM-Newton*, an ESA science mission with instruments and contributions directly funded by ESA Member States and NASA; the European Southern Observatory, Chile; Kitt Peak National Observatory, Cerro Tololo Inter-American Observatory, and the National Optical

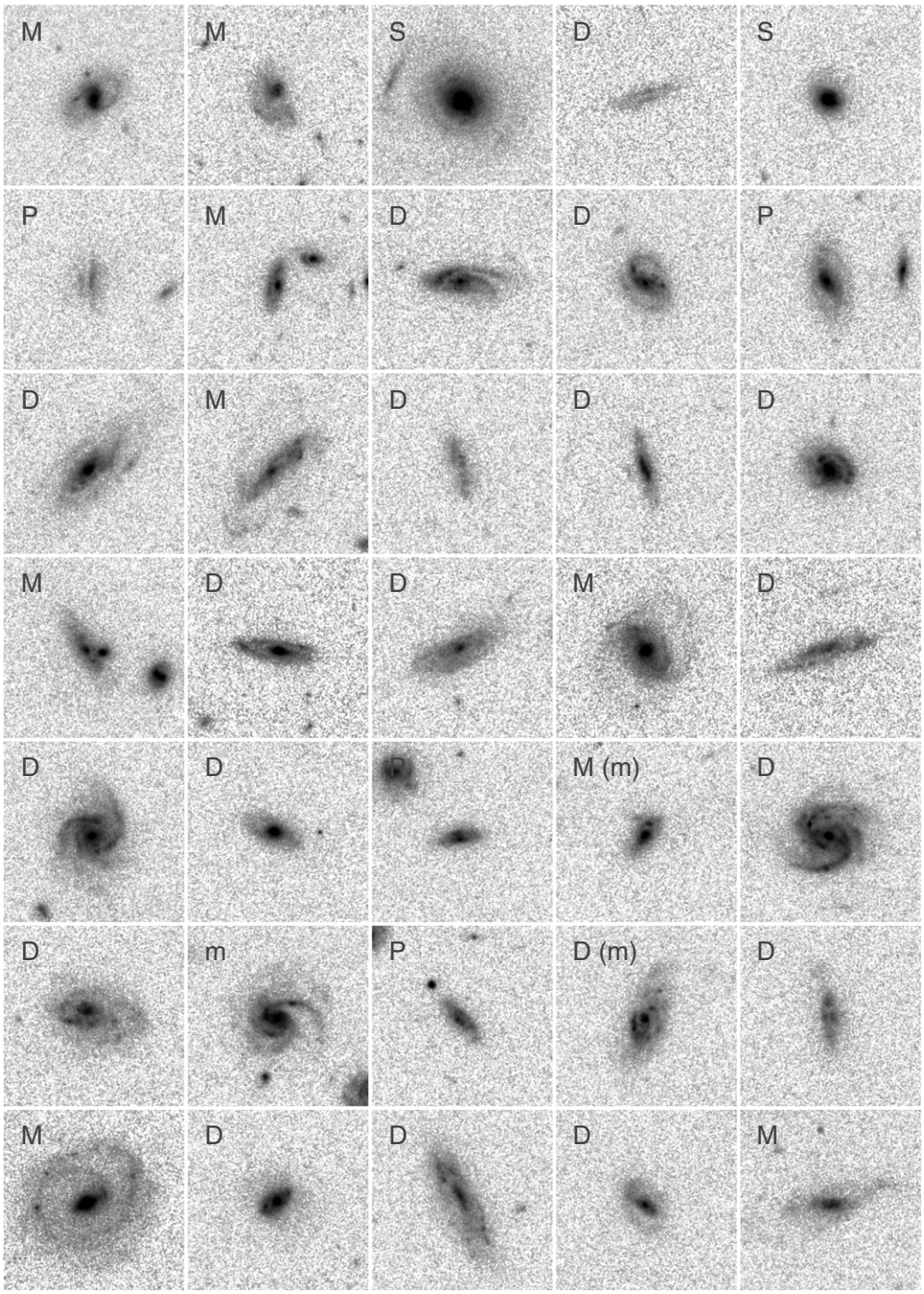

Figure 9. Same as Figure 8, galaxies at $0.65 < z < 0.72$ with $M_* > 10^{10.5}\,M_\odot$ and $10^{11.0} < L_{\rm IR} < 10^{11.5}\,L_\odot$.

Astronomy Observatory, which are operated by the Association of Universities for Research in Astronomy (AURA), Inc., under cooperative agreement with the National Science Foundation; the National Radio Astronomy Observatory, which is a facility of the National Science Foundation operated under cooperative agreement by Associated Universities, Inc.; and the Canada–France–Hawaii Telescope operated by the National Research Council of Canada, the Centre National de la Recherche Scientifique de France, and the University of Hawaii.

PACS has been developed by a consortium of institutes led by MPE (Germany) and including UVIE (Austria); KU Leuven, CSL, IMEC (Belgium); CEA, LAM (France); MPIA (Germany); INAF-IFSI/OAA/OAP/OAT, LENS, SISSA (Italy); and IAC (Spain). This development has been supported by the funding agencies BMVIT (Austria), ESA-PRODEX (Belgium), CEA/CNES (France), DLR (Germany), ASI/INAF (Italy), and CICYT/MCYT (Spain). SPIRE has been developed by a consortium of institutes led by Cardiff University (UK) and including University of Lethbridge (Canada); NAOC (China); CEA, LAM (France); IFSI, University of Padua (Italy); IAC (Spain); Stockholm Observatory (Sweden); Imperial College London, RAL, UCL-MSSL, UKATC, University of Sussex

(UK); and Caltech, JPL, NHSC, and University of Colorado (USA). This development has been supported by national funding agencies: CSA (Canada); NAOC (China); CEA, CNES, CNRS (France); ASI (Italy); MCINN (Spain); SNSB (Sweden); STFC (UK); and NASA (USA).

APPENDIX A

A. IMAGE GALLERY OF *HERSCHEL*-SELECTED GALAXIES

We present a subset of ACS images of *Herschel*-selected galaxies to demonstrate our visual classifications. However, we note that adjusting the brightness and contrast of these images has been a necessary step in our classification processes, which cannot be demonstrated in these fixed-stretch images. In Figures 8–11, we show a *randomly selected* subset of galaxies with $M_* > 10^{10.5}\,M_\odot$ in four $L_{\rm IR}$ bins. Due to the strong dependence between z and $L_{\rm IR}$, as demonstrated in Figure 1, the four $L_{\rm IR}$ bins have been chosen in slightly different redshift ranges.

We indicate our visual classification results in the top left corner of each image, with a possible alternative classification shown in brackets. We find that more than 80% of galaxies have clear conclusion of their classifications based on the discussion between three classifiers (C.L.H., D.B.S., and J.E.B.). For those

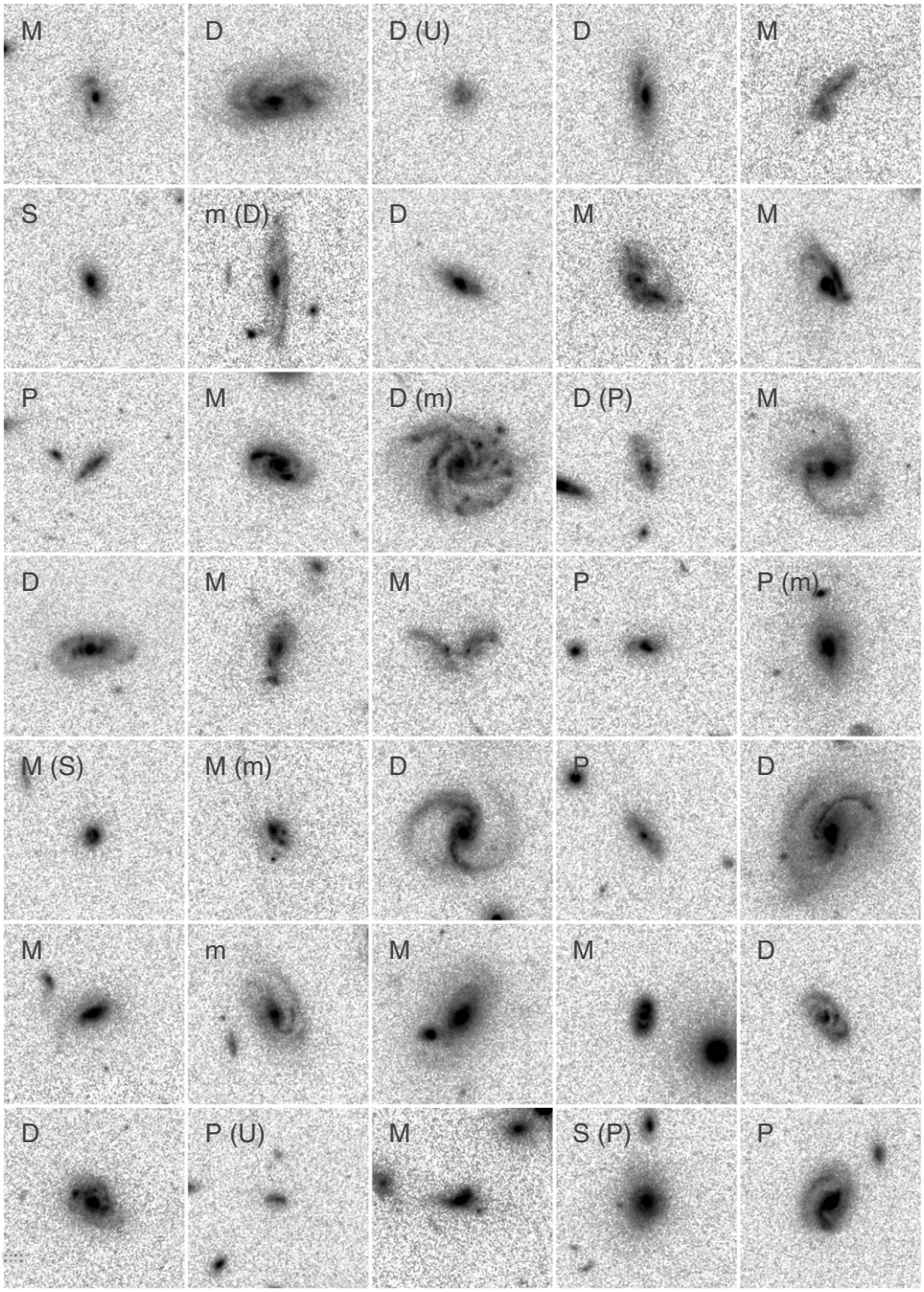

Figure 10. Same as Figure 8, galaxies at $0.67 < z < 0.72$ with $M_* > 10^{10.5}\,M_\odot$ and $10^{11.5} < L_{\rm IR} < 10^{12}\,L_\odot$.

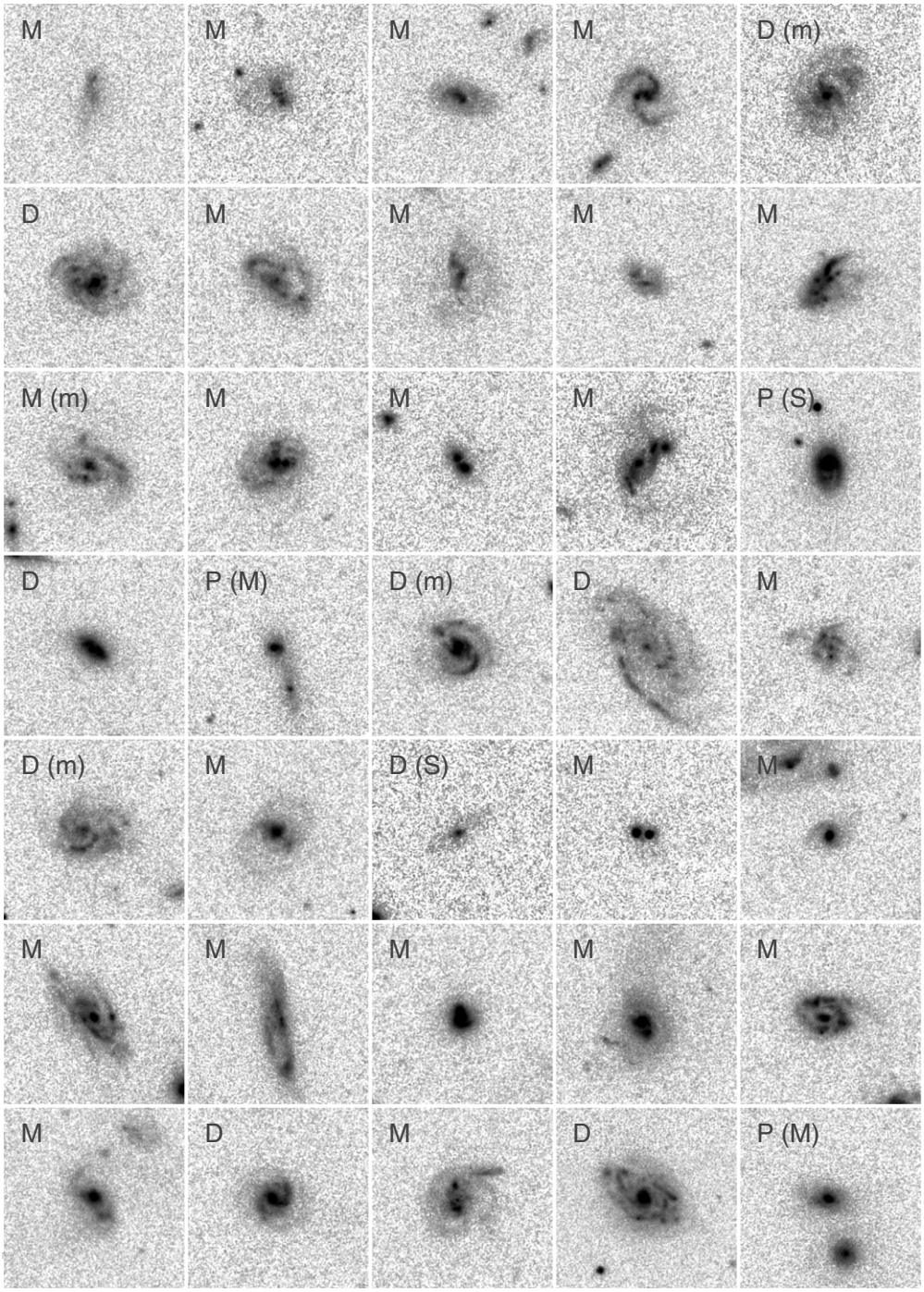

Figure 11. Same as Figure 8, galaxies at $0.65 < z < 0.95$ with $M_* > 10^{10.5}\ M_\odot$ and $L_{\rm IR} > 10^{12}\ L_\odot$.

~17% that may have alternative classifications, the confusion mostly originates in classifying non-interacting disks or minor interacting systems.

REFERENCES

Armus, L., Mazzarella, J. M., Evans, A. S., et al. 2009, PASP, 121, 559
Barnes, J. E., & Hernquist, L. 1992, ARA&A, 30, 705
Barnes, J. E., & Hernquist, L. 1996, ApJ, 471, 115
Berta, S., Magnelli, B., Nordon, R., et al. 2011, A&A, 532, A49
Bouché, N., Dekel, A., Genzel, R., et al. 2010, ApJ, 718, 1001
Brinchmann, J., Charlot, S., White, S. D. M., et al. 2004, MNRAS, 351, 1151
Cameron, E., Carollo, C. M., Oesch, P. A., et al. 2011, ApJ, 743, 146
Capak, P., Aussel, H., Ajiki, M., et al. 2007, ApJS, 172, 99
Casey, C. M. 2012, MNRAS, 425, 3094
Casey, C. M., Berta, S., Béthermin, M., et al. 2012, ApJ, 761, 140
Colina, L., Arribas, S., & Monreal-Ibero, A. 2005, ApJ, 621, 725
Davé, R., Finlator, K., Oppenheimer, B. D., et al. 2010, MNRAS, 404, 1355
Dekel, A., Birnboim, Y., Engel, G., et al. 2009a, Natur, 457, 451
Dekel, A., Sari, R., & Ceverino, D. 2009b, ApJ, 703, 785
Elbaz, D., Daddi, E., Le Borgne, D., et al. 2007, A&A, 468, 33
Ellison, S. L., Mendel, J. T., Scudder, J. M., Patton, D. R., & Palmer, M. J. D. 2013, MNRAS, 430, 3128
Elmegreen, D. M., Elmegreen, B. G., & Hirst, A. C. 2004, ApJL, 604, L21
Elmegreen, D. M., Elmegreen, B. G., Ravindranath, S., & Coe, D. A. 2007, ApJ, 658, 763
Förster Schreiber, N. M., Shapley, A. E., Erb, D. K., et al. 2011, ApJ, 731, 65
Griffin, M. J., Abergel, A., Abreu, A., et al. 2010, A&A, 518, L3
Grogin, N. A., Kocevski, D. D., Faber, S. M., et al. 2011, ApJS, 197, 35

Haan, S., Surace, J. A., Armus, L., et al. 2011, AJ, 141, 100
Hinshaw, G., Weiland, J. L., Hill, R. S., et al. 2009, ApJS, 180, 225
Hopkins, P. F., Hernquist, L., Cox, T. J., et al. 2006, ApJS, 163, 1
Howell, J. H., Armus, L., Mazzarella, J. M., et al. 2010, ApJ, 715, 572
Ilbert, O., Capak, P., Salvato, M., et al. 2009, ApJ, 690, 1236
Ilbert, O., Salvato, M., Le Floc'h, E., et al. 2010, ApJ, 709, 644
Ishida, C. M. 2004, PhD thesis, Univ. Hawaii
Kartaltepe, J. S., Dickinson, M., Alexander, D. M., et al. 2012, ApJ, 757, 23
Kartaltepe, J. S., Sanders, D. B., Le Floc'h, E., et al. 2010a, ApJ, 709, 572
Kartaltepe, J. S., Sanders, D. B., Le Floc'h, E., et al. 2010b, ApJ, 721, 98
Kennicutt, R. C., Jr. 1998, ARA&A, 36, 189
Kocevski, D. D., Faber, S. M., Mozena, M., et al. 2012, ApJ, 744, 148
Koekemoer, A. M., Aussel, H., Calzetti, D., et al. 2007, ApJS, 172, 196
Koekemoer, A. M., Faber, S. M., Ferguson, H. C., et al. 2011, ApJS, 197, 36
Koss, M., Mushotzky, R., Baumgartner, W., et al. 2013, ApJL, 765, L26
Lee, N., Sanders, D. B., Casey, C. M., et al. 2013, arXiv:1310.0474
Le Floc'h, E., Aussel, H., Ilbert, O., et al. 2009, ApJ, 703, 222
Le Floc'h, E., Papovich, C., Dole, H., et al. 2005, ApJ, 632, 169
Lotz, J. M., Primack, J., & Madau, P. 2004, AJ, 128, 163
Lutz, D., Poglitsch, A., Altieri, B., et al. 2011, A&A, 532, A90
McCracken, H. J., Capak, P., Salvato, M., et al. 2010, ApJ, 708, 202
Mihos, J. C., & Hernquist, L. 1996, ApJ, 464, 641
Noeske, K. G., Faber, S. M., Weiner, B. J., et al. 2007a, ApJL, 660, L47
Noeske, K. G., Weiner, B. J., Faber, S. M., et al. 2007b, ApJL, 660, L43
Oliver, S. J., Bock, J., Altieri, B., et al. 2012, MNRAS, 424, 1614
Pilbratt, G. L., Riedinger, J. R., Passvogel, T., et al. 2010, A&A, 518, L1
Poglitsch, A., Waelkens, C., Geis, N., et al. 2010, A&A, 518, L2
Rodighiero, G., Daddi, E., Baronchelli, I., et al. 2011, ApJL, 739, L40
Roseboom, I. G., Ivison, R. J., Greve, T. R., et al. 2012, MNRAS, 419, 2758
Roseboom, I. G., Oliver, S. J., Kunz, M., et al. 2010, MNRAS, 409, 48
Sanders, D. B., & Mirabel, I. F. 1996, ARA&A, 34, 749
Sanders, D. B., Soifer, B. T., Elias, J. H., et al. 1988, ApJ, 325, 74
Schinnerer, E., Sargent, M. T., Bondi, M., et al. 2010, ApJS, 188, 384
Scoville, N., Aussel, H., Brusa, M., et al. 2007, ApJS, 172, 1
Sérsic, J. L. 1963, BAAA, 6, 41
Stott, J. P., Sobral, D., Smail, I., et al. 2013, MNRAS, 430, 1158
Surace, J. A., Sanders, D. B., Vacca, W. D., Veilleux, S., & Mazzarella, J. M. 1998, ApJ, 492, 116
Toomre, A., & Toomre, J. 1972, ApJ, 178, 623
Veilleux, S., Kim, D.-C., & Sanders, D. B. 2002, ApJS, 143, 315
Veilleux, S., Kim, D.-C., Sanders, D. B., Mazzarella, J. M., & Soifer, B. T. 1995, ApJS, 98, 171
White, S. D. M., & Rees, M. J. 1978, MNRAS, 183, 341
Wuyts, S., Förster Schreiber, N. M., Lutz, D., et al. 2011a, ApJ, 738, 106
Wuyts, S., Förster Schreiber, N. M., van der Wel, A., et al. 2011b, ApJ, 742, 96